Investigations on dynamic water transport characteristics in flow field channels using neutron imaging techniques

M. Klages [a],[*], S. Enz [a], H. Markötter [b], I. Manke [b], N. Kardjilov [b], J. Scholta [a]

[a] Zentrum für Sonnenenergie- und Wasserstoff-Forschung Baden-Württemberg (ZSW), Helmholtzstr. 8, 89081 Ulm, Germany
[b] Helmholtz-Zentrum Berlin für Materialien und Energie GmbH (HZB), Hahn-Meitner-Platz 1, 14109 Berlin, Germany

HIGHLIGHTS

► Three basic flow field designs are investigated: pattern structure, meander-shaped channels, straight channels.
► Flow fields are compared regarding power and water inventory.
► Water thicknesses under channel and under land are separately calculated.
► Results of neutron radiography and CFD simulation are combined.
► A condensate removal criterion of 20 mbar m^{-1} is proven.

GRAPHICAL ABSTRACT
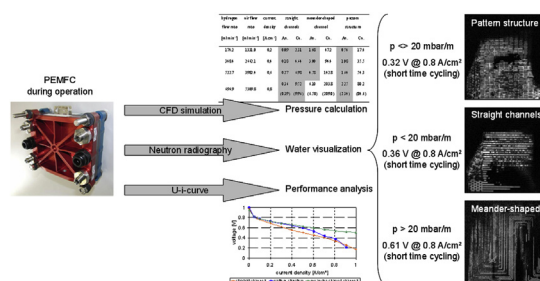
ABSTRACT

Handling of water accumulation is still a key issue in fuel cell research. The presented study evaluates the condensate removal capability of three different flow field designs. The designs are compared regarding cell voltage at different current densities using the same operating conditions. The investigated type of meander-shaped channels with a high degree of parallelization shows the best performance with stationary water thickness inside channels throughout the analyzed current densities. To develop and evaluate a condensate removal criterion for fuel cell construction, the pressure drop of each flow field is correlated to the water appearance visualized with neutron radiography. For a further insight, computational fluid dynamics simulation is used to calculate pressure drops present inside the characteristic regions of each flow field. Thus, a characteristic design limit of 20 mbar m^{-1} for meander-shaped channels is proven to ensure the absence of channel blockage. The meander-shaped channels show specific pressure drops around this limit depending on water production and gas supply. The two other analyzed flow fields suffer from higher channel filling rates: the investigated straight channels with less parallelization fill up with time, while the pattern-structured flow field demonstrates gravity as an additional influence on condensate removal.

© 2013 Elsevier B.V. All rights reserved.

1. Introduction

Low temperature polymer electrolyte membrane fuel cells (PEMFCs) offer a great potential for a broad range of applications because of their technical maturity and durability [1–3]. Nonetheless, one of the most important challenges for commercialization is an appropriate water management in order to achieve reliable performance and high power output [4]. Good membrane proton conductivity needs a high amount of water present inside the fuel cell, whereas too much water results in flooding of gas diffusion layers (GDLs) and blocking of channels [5] leading to lower performance and degradation effects [6].

* Corresponding author. Tel.: +49 731 9530 209; fax: +49 731 9530 666.
E-mail address: merle.klages@zsw-bw.de (M. Klages).

In literature, there is more than one parameter to evaluate condensate removal capability. Some work was done correlating droplet movement to the Reynolds number of a channel at particular air flow rates in order to predict water removal [7]. Other dimensionless values, like Laplace number or Weber number, can be used to evaluate multi-phase flow [8]. The driving force of the water movement inside the flow field channels is the pressure difference between gas inlet and outlet. Thus, the pressure drop between inlet and outlet is a powerful parameter to optimize fuel cell design. Chen and Zhou correlated the time dependency of pressure drops to a voltage decrease because of flooding. They propose to measure the frequency in pressure change for the diagnosis in fuel cell operation [9]. Spernjak et al. investigated the pressure of a parallel and a single-serpentine flow field to evaluate the water accumulation. The parallel flow field showed a low pressure difference in combination with an unstable performance, whereas the single-serpentine flow field showed overall a four times lower water content and higher performance [10].

One developmental issue that remained open so far is the combination of low pressure drop on one hand and good condensate removal capability on the other hand. In previous research activities, the condensate removal capability of flow field channels was investigated both ex-situ for single straight channels [6] and in-situ for parallel or serpentine flow fields [11]. The ex-situ investigations were performed using a graphite composite material covered and sealed by a transparent endplate. Thus, the influence of channel geometry on the water transport ability could be seen. Since this procedure is not possible, if the channel is covered with a GDL, other methods have to be used to characterize the water removal characteristics. In Ref. [11], in-situ condensate removal behavior was investigated by indirect methods like pressure drop changes and gas utilization curves.

Before performing utilization curves, an overall condensate removal criterion using a simulation can be calculated. A simulation of the flow field before the actual manufacturing is often used to predict fuel cell performance simultaneously reducing development costs. There are different custom-designed tools and different models. The software used within the presented study is ANSYS® FLUENT®. Further studies using a three-dimensional simulation are described e.g. in Refs. [12–14].

In the past, imaging methods based on X-rays and neutrons were frequently used for the visualization of water distribution in fuel cells under operation [15–17,37]. The purpose of the presented study is to extend recent fuel cell investigations by in-situ diagnostics during fuel cell operation which can be performed using neutron radiography. Several investigations using neutron radiography and tomography on water transport in flow fields proved the applicability of this method [18–20]. In this study a detailed examination of the condensate removal behavior with respect to pressure drop is performed.

2. Experimental

Three basic structures in flow field design with different magnitudes of pressure drop were investigated regarding power and condensate removal: pattern flow field, meander-shaped and straight channels. Each channel had a rectangular cross section. Fig. 2 shows the design sheets of the flow fields. The same design was used on both anode and cathode side in order to evaluate both sides of a fuel cell regarding condensate removal capability at the same time and in the same way. As the fuel cells were operated in counter-wise gas direction, anode and cathode flow fields were horizontally flipped. The meanders and the pattern structure had a high degree of parallelization. The cross-sectional area for these flow fields was 0.36 mm² and 1.2 mm² for the parallel flow field.

The width of the straight channels was more than doubled compared to the other two designs. This flow field had 40 straight channels. Table 1 summarizes the characteristics of the investigated flow field designs used within this study. The specified designs were investigated with neutron radiography (2.1) and a simulation was performed to get a further insight (2.2).

2.1. Neutron radiography procedure

From previous studies neutron radiography turned out to be very suitable to detect and quantify water clusters while allowing an investigation of the whole active area of 100 cm² [21–23]. Neutron imaging was carried out at the CONRAD/V7 facility of the Helmholtz-Zentrum Berlin (BER II research reactor). Experimental details of the setups for the neutron imaging technique used for this study can be found in Refs. [24–26]. To analyze the dynamics of water evolution and transport, the exposure time and the readout time were minimized down to 3 s and 2 s, respectively. As time and spatial resolution conflict, the radiographs were taken with 100 μm per pixel using a ^{6}LiZnS scintillator with a thickness of 200 μm. As the water inside the gas channels is the main object of investigation, this pixel size is sufficient. With a longer exposure time, a spatial resolution down to 25 μm per pixel is possible in neutron imaging [22]. The water content of a fuel cell is highly influenced by the amount of water production through the electrochemical reaction as well as the condensate removal capability. To analyze the dynamic water characteristics inside the flow field, current density and thus gas flow rate at constant utilization was varied with short holding times of 3 min. Within this time, current density was varied within the range of 0.2 A cm^{-2} and 0.8 A cm^{-2}. These current densities correspond to a high and a low voltage level of the investigated fuel cells. The operating conditions are shown in Table 2. All fuel cells contained the same GDL (Sigracet® SGL 10BC) as well as the same membrane electrode assembly (GORE™ PRIMEA® 5761).

2.2. Parameters for CFD simulation

Neutron radiography can be used to identify critical flow rates causing blockage of channels as well as a further investigation of the shape of water accumulations, like slug or droplet formation. The different shapes are described e.g. in Ref. [27]. For the development and optimization of fuel cells neutron radiography in combination with computational fluid dynamics (CFD) simulation are tools of growing interest. Simulation can be additionally consulted if operating parameters cannot be measured, like pressure distributions throughout single channels, or are within tolerance of measurement instruments. On the other hand, neutron radiography helps to verify simulation results predicting e.g. the condensation of water. Within this study, for mechanisms that cannot be studied under real in-situ conditions ANSYS® FLUENT® (version 13.0) was used. For the performed half cell simulations, anode as well as cathode geometry consisting of flow field, GDL

Table 1
Characteristics of the flow field designs.

	Meander	Straight	Pattern
Land width	0.8 mm	1.0 mm	5.0/1.0 mm
Channel width	0.6 mm	1.5 mm	0.6 mm
Channel depth	0.6 mm	0.8 mm	0.6 mm
Number of channels	23	40	63 horizontal, 10 vertical
Cross-sectional area	0.36 mm²	1.2 mm²	0.36 mm² horizontal, 0.6 mm² vertical
Specific channel length	301.7 mm	61 mm	61 mm

Table 2
Operating conditions during neutron measurements.

Operating parameter	Value
Cell number	1
Fuel cell temperature	60 °C
Utilization cathode; anode	25%; 80%
Anode gas	Hydrogen
Relative humidity cathode; anode	26%; 0%
Current densities	0.2; 0.4; 0.6; 0.8 A cm^{-2}
Holding time	3 min
Direction of gas flow	Counter flow

(also the micro porous layer), and catalyst layer were generated with ANSYS® DesignModeler™ and discretized with ANSYS® Meshing™. The mesh generation was accomplished with the "sweep algorithm" which uses hexahedrons as finite volume elements resulting in a total number of 5–6 million elements per geometry. Each flow field was meshed with 5 elements, GDL with 4 elements and catalyst with 1 element over the height. Each flow field channel contains 5 elements over the width. In order to simulate the electrochemical reactions at the catalyst layer, constant source terms according to the provided current density were used. For more details of the simulation may be referred to Refs. [28,29]. Basic approaches of the simulation presented in this study can be found e.g. in Refs. [30,31].

Table 3 summarizes the operating conditions having served as inputs for the simulation. Within the acknowledged project the focus lies on the neutron investigation. The simulation, used for additional information, was performed for different operating conditions to get a broad application range. However, with some corrective changes the simulation is also applicable for the operating conditions shown in Table 2. A correction factor of the pressure p was implemented representing the ratio of the average molar flow rates n of the simulation and the experiment (see equation (1)). The maximum Reynolds numbers of the cathode sides of each simulation shown in Table 4 in brackets for pattern structure, meander-shaped and straight channels are 303, 285 and 353. As these values are lower than the critical Reynolds number of 2300, a model for laminar flow is used. The pressure drop of a laminar flow, which is predominantly present in PEMFC channels, is directly proportional to the velocity. The velocity can be expressed as the product of the molar flow rate and the molar volume of an ideal gas divided by the cross-sectional area of the gas channel. A correlation between pressure drop and molar flow is mentioned e.g. in Ref. [32]. As the channels simulated and experimentally investigated had the same geometry (length, width and height) and for the simulation no phase change is considered, the molar flow rates and thus the pressure do only depend on the operating conditions. The flow rates consisting of water vapor and gas stream were calculated depending on current density, gas utilization, gas composition and inlet gas humidification. The particular terms were calculated according to [33]. The water input by gas humidification is calculated using the Antoine equation. The pressure $p_{simulation}$ in equation (1) is the pressure calculated for the operating conditions shown in Table 3 converted to pure hydrogen

Table 3
Input parameters for the CFD simulation.

Operating parameter	Value
Cell number	1
Fuel cell temperature	75 °C
Utilization cathode; anode	60%; 75%
Anode gas composition hydrogen:nitrogen	65 vol-%:35 vol-%
Relative humidity cathode and anode	80%
Current density	0.2–1.0 A cm^{-2}

usage regarding the reformate composition. Section 3.5 shows a comparison between the calculated pressure drops and an additional simulation with the operating conditions listed in Table 2.

$$p_{experiment} = p_{simulation} \cdot \frac{1/2 \cdot (n_{in} + n_{out})_{experiment}}{1/2 \cdot (n_{in} + n_{out})_{simulation}} \tag{1}$$

3. Results and discussion

Neutron radiography provides an integral view of anode and cathode side, i.e. the sum of the water content along the neutron beam imaging the active area of 100 cm^2. As the channels on both anode and cathode side basically superpose a separation of the integral water content to land and channel regions can be done easily. The mathematical separation of the water content is done using the original CAD data sheets to mask either the region under the land or under the channels. The method of masking is described in detail in Ref. [34]. In the following, the calculated average water thickness under the land represents the sum of the water content of the membrane electrode assembly as well as inside the GDLs under the lands of the flow field for the whole active area. The water thicknesses in the GDL under the channels depend on the water content of the channels nearby and vice versa. Fig. 1 exemplifies the water distribution for eighteen channels in the middle of the flow field with meander-shaped channels at a current density of 0.8 A cm^{-2}. The water content in the GDL under empty channels is 0.038 mm lower than under the lands nearby indicating lower water content under the channels limited by a proportion of 36.2% as a result of the gas stream carrying the water along. This estimation is done using meander-shaped channels as this flow field has the highest amount of empty channels during the performed measurement procedure. Higher water contents of the GDL under the lands compared to the channels can also be seen using X-ray tomography, e.g. in Ref. [35]. As water is continuously transported through the fuel cell channels, a precise calculation of the water content in the GDL under the filled channels as a measurement of the actual humidity of the gas stream is not possible in radiography. The difference of the water thicknesses under the channels and under the lands gives an impression of the minimum water content present in the gas stream. One has to keep in mind that the water thickness in the GDL can vary down to two-thirds of the values under the lands shown in the following graphs. The water thicknesses shown in Figs. 4–7 represent the actual thicknesses under the channels without any mathematical subtraction and thus include water in GDL and channels. The correlation to anode and cathode side is done by either the water flow direction (meander-shaped channels) or the shape of the pattern-structured parts in the gas inlet and outlet region visible in Fig. 2 (pattern and parallel flow field). Fig. 3 shows exemplarily some radiographs of the three flow field designs. The maximum water content is colored in white and the thickness is calculated according to Lambert Beer's law within mm-scale (see calibration bar in each image). The procedure for the water calculation is described e.g. in Ref. [36]. The pattern-structured parts in the gas inlet and outlet regions are highlighted for a further correlation of the water content to anode and cathode side. Additionally, in Fig. 3 single channels in the middle of each flow field are highlighted which will be further investigated in the following.

3.1. Water content inside the pattern-structured flow field

The flow field with pattern structure shows an increasing water thickness in the channels and inside the GDLs with measurement time (see Fig. 4). The measurement procedure consists of various

Table 4
Adjusted and simulated specific pressure drops [mbar m^{-1}] over the specific regions for operating conditions during neutron radiography (simulated pressure drops in brackets).

Hydrogen flow rate [ml min^{-1}]	Air flow rate [ml min^{-1}]	Current density [A cm^{-2}]	Straight channels		Meander-shaped channels		Pattern structure	
			An	Ca	An	Ca	An	Ca
174.2	1331.0	0.2	0.09	2.31	1.48	47.2	0.54	17.4
348.4	2662.1	0.4	0.18	4.64	3.00	94.4	1.08	35.5
522.7	3982.4	0.6	0.27	6.98	4.58	142.8	1.64	54.3
696.9	5309.8	0.8	0.36 (0.39)	9.52 (9.96)	6.10 (6.50)	203.8 (209.0)	2.25 (2.34)	80.2 (84.6)

steps with increasing current density and thus an increasing water production rate. After a period of 38 min equilibrium is reached: 0.20 mm under the channels and 0.12 mm under the lands. The gradient in water increase depends basically on the water production rate, visible up to minute 87. While the water thicknesses are increasing the voltage is decreasing within the same time. At equilibrium, there are voltages of 0.73 ± 0.01 V at 0.2 A cm^{-2} and 0.32 ± 0.02 V at 0.8 A cm^{-2}. Regarding the image sequences, there are film and droplet formation on both anode and cathode side. Condensate removal is dominated by gravity. That means, the water accumulates among the vertical and horizontal channels and moves downwards as soon as a particular amount is reached. From the lower part of the flow field the water is transported in both directions to the gas outlets. The pattern structure of the anode outlet design on the right side of the flow field can be clearly identified (see left image in Fig. 3). The absence of the cathode pattern structure in this region indicates that the water on the cathode side is successfully removed. If the cathode had condensate removal problems, the water would accumulate before entering the middle structure of the flow field with the characteristic length. In contrary, the pattern structure on the left side shows characteristics of anode and cathode design, representing condensate removal problems on the anode side. That means anodic water accumulates in the left region near the anode gas inlet before passing the characteristic structure of the middle part. Assuming the total water thickness under the channels less the total water thickness under the lands corresponds to the anode flow field there is an average filling rate of 13.4% of one channel depth. Assuming that the filling of the GDL is reduced by 36.2% under the channels, the filling rate adds up to a higher level of around 20.8%.

3.2. Water content inside the flow field with straight channels

Equilibrium in water thicknesses, as seen when using the pattern structure, is not reached for the case of straight channels for the performed operating conditions. With measurement time the filling level of the channels is increasing while the voltage is decreasing (see Fig. 5). Within the experiment duration of about 75 min no stationary voltage is achieved. At the end of this time, there is a still decreasing voltage of 0.73 V at 0.2 A cm^{-2} and 0.36 V at 0.8 A cm^{-2}. The cathode channels show slug formation without complete filling of the channel depth, which is a sign for inadequate condensate removal. The water accumulates along the horizontal channel length from the left to the right side of the radiographs and fills up the channel as it does not exit the characteristic part of the parallel flow field design. The lower left part of the radiograph in Fig. 3 clearly shows the anodic pattern design, indicating an accumulation of anodic water before the characteristic part of the flow field. As the water does not pass the straight channels throughout the full height of the fuel cell, the water accumulates on the bottom of the flow field and is transported through the lower few channels with the gas stream (see the direction of arrows in Fig. 3). Both anode and cathode condensate removal capability of the investigated type of parallel flow field design (channel length, cross-sectional area) is insufficient: whereas the cathode water mainly accumulates in the middle region, the anodic water is even blocked before entering this region. Although the channels are not completely blocked, the gas supply of the active area is severely limited indicated by a decreasing voltage with time. The water thickness under the lands in Fig. 5 is averaged over the characteristic part and does not include the anodic water accumulation in the pattern structure, but in the lower few channels.

3.3. Water content inside the flow field with meander-shaped channels

The filling level of the meander-shaped flow field is overall less than for the other two designs. Fig. 6 displays the measurement period with short time cycling between 0.2 and 0.8 A cm^{-2}. There are equal voltage levels at the same amount of current density
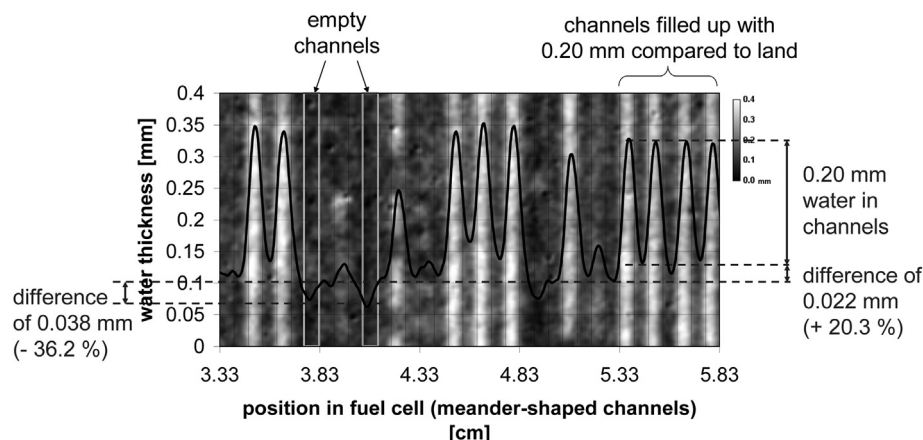
Fig. 1. Water thickness under channel and under land in the middle of the fuel cell with meander-shaped channels in minute 77.9 of Fig. 6.
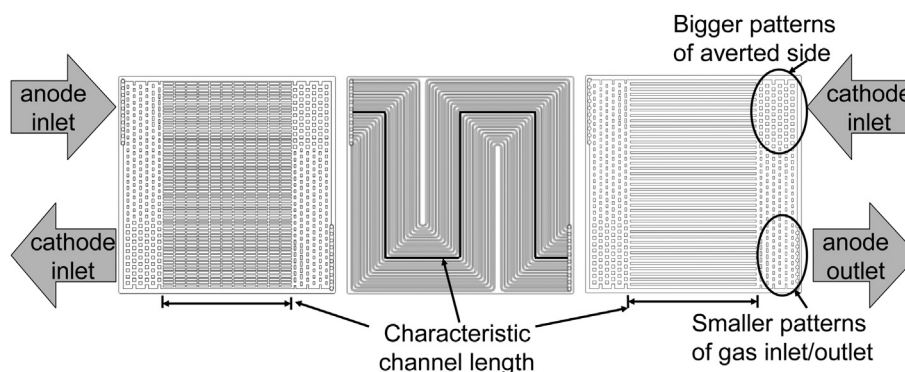
Fig. 2. CAD sheet of the investigated anode flow fields with gas flow direction and characteristic channel length.

during step procedure: 0.77 $\pm$ 0.01 V at 0.2 A cm^{-2} and 0.61 $\pm$ 0.01 V at 0.8 A cm^{-2}, which is higher as for the case of the other investigated flow field designs. Fig. 6 shows similar water thicknesses during measurement time. Regarding the water movement in the radiographic sequence, the water accumulation can be allocated mainly to the anode side. Especially at 0.2 A cm^{-2}, there is an overall water accumulation in the anodic channels which is a sign for inadequate condensate removal. In addition, the water accumulation of the middle part in Fig. 3 remains inside the channels in upwards gas flow direction due to gravity. The evolution of small water droplets on the cathode side by the electrochemical reaction can be seen at low air flow rates. At overall high volume flow rates despite a high water production at a current density of 0.8 A cm^{-2}, the water on the cathode side is removed sufficiently. The anodic water, aggregated during fuel cell operation at 0.2 A cm^{-2}, is sufficiently removed, when turning up the gas flow rate corresponding to a current density of 0.8 A cm^{-2}.

3.4. Spatially resolved investigation of single channels

The above shown average water thicknesses under channels and lands of the whole active area give an insight into the overall difference in water content. Not only because of the gravity influence on water accumulation in different regions of a flow field, the actual thicknesses under the channels have to be examined in order to evaluate the shape of water formation and movement. Fig. 7 exemplifies representative filling levels in single channels in the middle of each flow field at a current density of 0.8 A cm^{-2}. The water thicknesses are calculated as average values over the

channel width in horizontal direction for the pattern structure as well as the straight channel and in vertical direction for the meander-shaped channel (see highlighted regions in Fig. 3). The total length of the abscissa matches the width of the active area of 10 cm. Between the positions 4 and 7 cm, the average water thickness in the pattern-structured flow field is about 0.34 $\pm$ 0.03 mm, which corresponds to a filling rate of around 57% compared to one channel depth disregarding a filling of the GDL under the channel. Averaging between 2 and 7 cm, the water thickness adds up to 0.38 $\pm$ 0.08 mm, which is caused by the accumulation of water before the actual removal by gravity. Within the positions 1 and 7 the meander-shaped channel has a uniform water distribution of 0.33 $\pm$ 0.03 mm, which corresponds to the water thickness of the pattern structure at equilibrium. Both flow fields have a high grade of parallelization and a similar cross-sectional area. The line drawn for the calculation of water thicknesses intersects a few more channels which also reach a water thickness of roughly 0.33 mm (see positions 0.43, 0.71 and 0.86). The exemplary straight channel shows an increase in water thickness in the direction from the cathode gas inlet to the outlet because of the increase in relative gas humidity by the electrochemical reaction. The single straight channel represents a slug formation on the cathode side (gray) and the droplet formation on the anode side (white). The regression line drawn for the slug formation shows a difference of 0.15 mm between 2.3 and 7.4 cm, which can be correlated to filling rates between 66 and 83%. The sum of both anode and cathode channel adds up to a maximum of 0.9 mm, i.e. a droplet formation with a thickness up to 0.2 mm on anode side. The anodic water accumulating in the left region of the
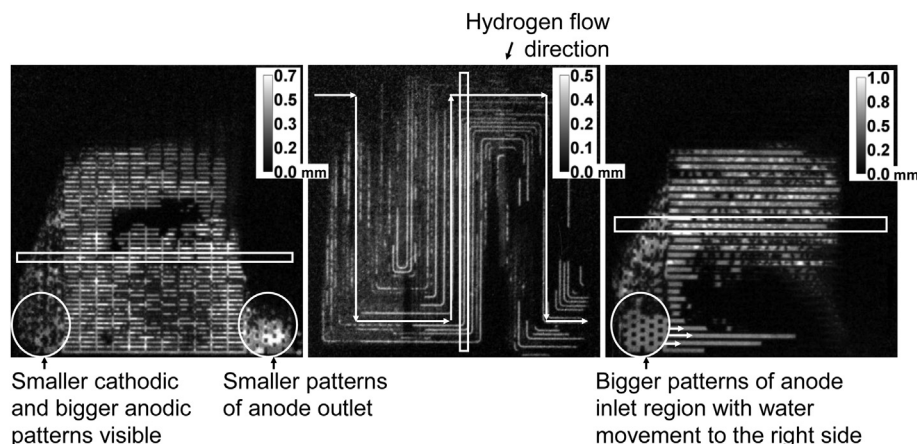

Fig. 3. Radiographs of the investigated flow field designs (from left to right: pattern structure, meander-shaped flow field, straight channels) with calculated water thickness in mm.
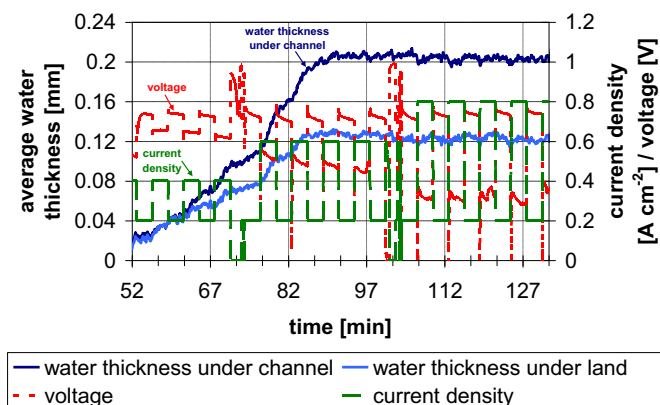
Fig. 4. Average water thickness in flow field with pattern structure.

Fig. 6. Average water thickness in flow field with meander-shaped channels.

flow field and being removed through the lower horizontal channels is not displayed in Fig. 7.

3.5. Combination of condensate removal and simulated pressure drops

In order to develop or evaluate a condensate removal criterion, the pressure drop can be correlated to the appearance of liquid water using neutron radiography. Table 4 summarizes the calculated specific pressure drops of the three flow field designs. The specific pressure drop represents the difference between the entrance and the outflow of the specific region divided by the length. In contrary to the experimental results, the simulation provides the pressures inside each flow field structure. The segments emphazised with italic in Table 4 represent operating conditions without sufficient water removal. This means, neutron radiographs show water formation as stationary droplets or water lines with sparse motion. For a better comparability, the pressure drops are related to the specific channel lengths. In case of the meander-shaped channels the small manifold region is negligibly small. The specific length corresponds to the length of the middle channel. As the other two flow field designs have an additional structure of small patterns in the gas inlet and outlet regions, only the inner part is taken into account as this is the limiting region for condensate removal.

To verify the values of the calculated pressure drops and thus the conversion explained in Section 2.2, an additional simulation with the operating conditions of Table 2 was performed. The pressures inside the three different flow field designs were
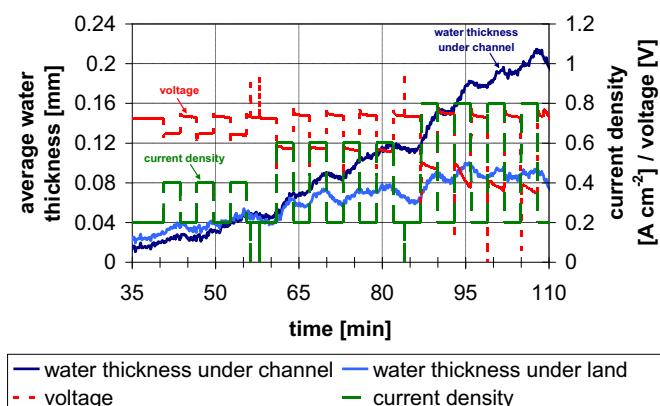
calculated for the maximum current density of 0.8 A cm^{-2}, as the maximum deviation is expected for the maximum flow rates. The additional values are shown in Table 4 in brackets. Adjusted and calculated values are within the same range for each flow field.

Table 4 shows the pressure values over the specific length. In Figs. 8 and 9, the calculated pressure drop between fuel cell gas inlet and outlet is compared to the experimentally measured pressure drops during voltage–current density-curves, as the experiments cannot depict the pressures inside the channels. The total anodic pressures of the flow fields with pattern structure and straight channels are below the minimum pressure of the manometers installed at gas inlet and outlet. The pressure drops of the fuel cell with meander-shaped channels can be compared best to the simulation as the manifold region is small and also the pressures on the anode side at a current density above 0.6 A cm^{-2} can be actually measured. The pressure drop on the anode side at a current density below 0.6 A cm^{-2} is beneath the resolution limit of the manometers. The voltage–current density-curves are performed with the operating conditions shown in Table 2 and holding times of 20 min for each current density step. To calculate the pressure difference between fuel cell gas inlet and outlet a prior experiment without the fuel cell was performed to measure the pressure drop of the test bench. Fig. 8 shows a comparison of the anodic and cathode pressure drops between gas inlet and outlet for the meander-shaped channels. In the simulation the relative gas
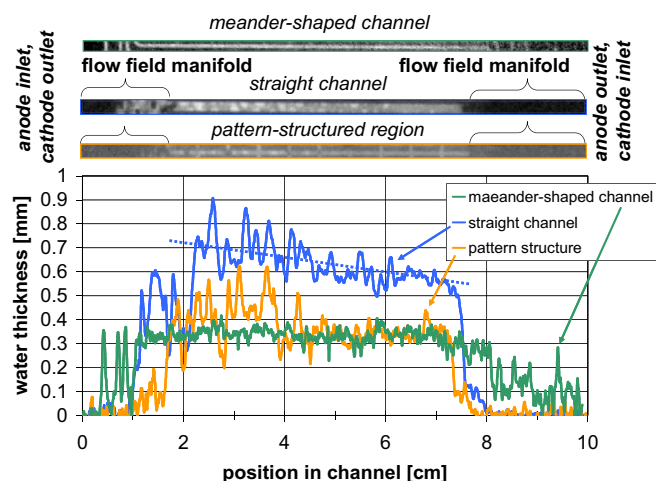

Fig. 5. Average water thickness in flow field with straight channels.

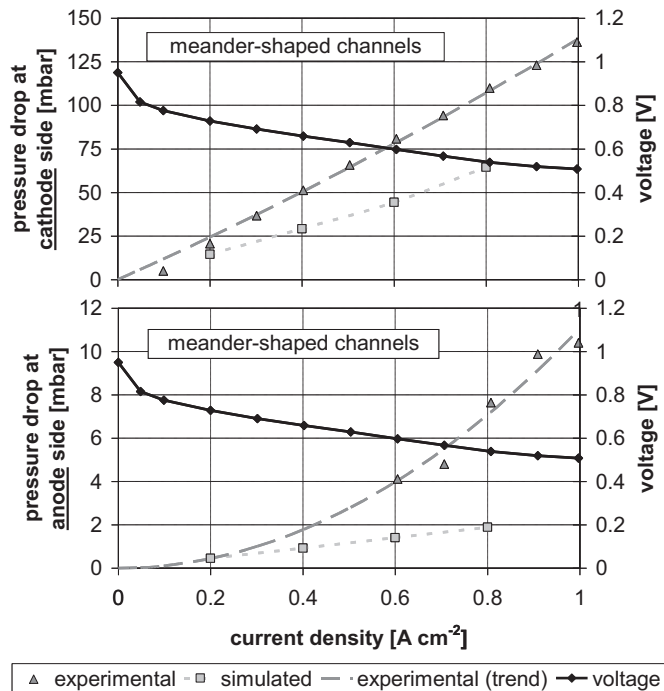**Fig. 7.** Water thickness in exemplary single channels at 0.8 A cm^{-2}.

Fig. 8. Comparison of the experimentally determined and the simulated pressure drop between gas inlet and gas outlet in mbar of the fuel cell with meander-shaped channels.

humidity is considered as molecules within the gas stream, but no liquid state of aggregation is taken into account. This means, the pressure drop of a flow field is not increased by the presence of liquid water. Due to condensate formation the experimental pressure drop is higher than simulated. For the cathode side the factor is 1.7, for the anode side 3.4. As the flow field for the anodic operating conditions offers a lower condensate removal capability than the cathode side, the higher factor for the anode side is expectable (see

Fig. 9. Cathode pressure drops of the flow field with straight channels (top) and with pattern structure (bottom).

Section 3.3). Multiplying the specific pressure drops displayed in Table 4 with the factors for anode and cathode side mentioned above, results in a minimum cathode pressure drop of 80.9 mbar m^{-1} at 0.2 A cm^{-2}. For the anode side, at a current density of 0.6 A cm^{-2}, there is an adjusted specific pressure drop of 13.2 mbar m^{-1} in combination with observable water accumulation. For 0.8 A cm^{-2} the pressure drop adds up to 23.3 mbar m^{-1} in combination with sufficient condensate removal. Taking the condensate appearance observed with neutron radiography into account, roughly 20 mbar m^{-1} [38] as the critical criterion for condensate removal is proven for meander-shaped channels.

Fig. 5 displays a steadily increase in water thickness in combination with a decrease of voltage for the design with straight channels. This means, that within the experienced operating conditions and in horizontal orientation of the channels this type of flow field has overall problems in condensate removal. The correlation of pressure drop and water appearance of the pattern flow field is more complex. The water content in the flow field increases up to an equilibrium. Solely the gradient of water increase dependents on the current density, but not the amount of water at equilibrium. The water can basically be seen on the anode side and is not removed with the gas flow rate, but with gravity. Thus, the anodic channels are the dominating side for further optimization of condensate removal. As the water on the cathode side appears as moving droplets, there seems to be a sufficient water removal. Fig. 9 displays the cathode pressure differences for the pattern structure and the straight channels. Regarding Figs. 8 and 9, it can be concluded, that simulated and measured pressure drops follow the same trend with a higher experimental pressure difference. On the cathode side, the experimental pressures of the meander-shaped and the pattern-structured channels are roughly doubled compared to the simulation. The absence of a phase change is the presumably reason for the increasing gap between simulation and experiment with increasing current density. The fuel cell with straight channels shows a higher deviation than the other two flow fields caused by the rise in slug formation with increasing current density blocking parts of the cross-sectional channel area (see Fig. 9). Another difference between simulation and experiment is the absence of the electro-osmotic drag from anode to cathode within the performed simulation, which leads to somewhat higher simulated pressures at the anode and corresponding lower values at the cathode. As a half cell simulation was performed, anode and cathode are not physically connected by a membrane. Thus, an actual water transport is not considered. The authors chose a half cell simulation due to simplicity of simulation geometry and requirements on computer performance to calculate the pressure values. Concluding, a CFD simulation gives a good insight into condensate removal capability before the actual manufacturing process, but an experimental verification of the results provides the actual values. However, as the difference between simulation and experiment follows the same trend for all investigated flow field designs the critical value of 20 mbar m^{-1} can be reasonably used for an estimation of condensate removal.

The investigation is performed with graphite based bipolar plates, which show a contact angle of approximately 80° [39] influencing the droplet removal behavior. The presented study covers a channel cross-sectional area ranging from 0.36 to 1.2 mm^2. There are experimental hints that the developed condensate removal criterion is valid up to a cross-sectional area of 1.5 mm^2. Up to now, no statement can be made on channel geometries with lower or higher cross-sectional area. This and the comparative analysis of droplet movement data derived from theory [40], ex-situ [6,7] and in-situ studies [11,41] as well as for simulations [42,43] with respect to the pressure drop criterion shall be investigated in future work.
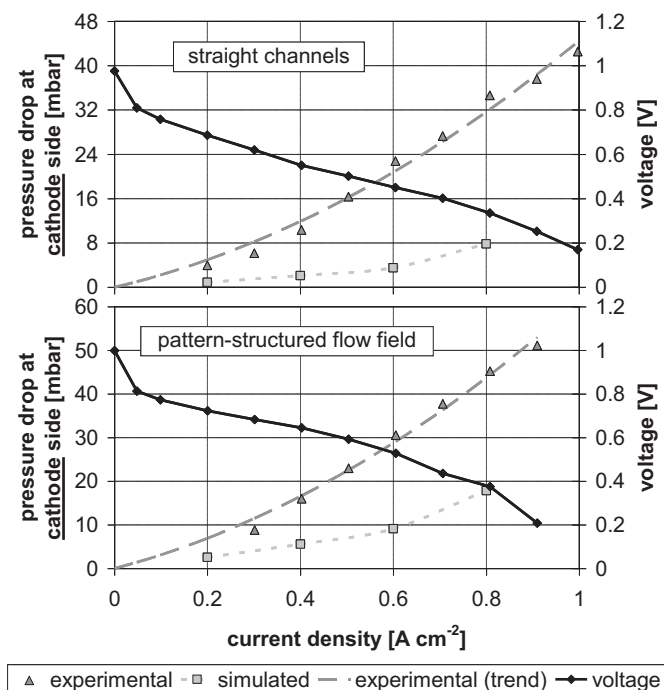
4. Conclusions

In the performed neutron radiography experiments no filling rates of 100% for the channels are observed, i.e. there is still enough space for a minimum of gas supply at least for the applied operating conditions. However, insufficient condensate removal is observed for some flow fields at particular operating conditions allowing the evaluation and development of limiting criteria for condensate removal to optimize fuel cell design.

In comparison, the design of the meander-shaped flow field shows a stationary high power output in combination with almost constant water content, while the fuel cell with the pattern flow field yields only 0.32 V at 0.8 A cm^{-2}. Spatially resolved investigation shows a similar water thickness of around 0.3 mm for both designs. The meander-shaped flow field with high specific pressure drops shows the best condensate removal capability. From neutron radiography measurements it can be concluded that water is basically formed at the anode side and removed with high gas flow rates. For this flow field a condensate removal criterion is proven. The fuel cells with the other two investigated designs exemplify a continuously decreasing voltage of fuel cells with overall low pressure drop. Straight channels with relatively high cross-sectional area and corresponding low pressure drop show slug formation visible at low and high current density for the chosen gas utilizations.

Acknowledgment

References

[1] W. Vielstich, A. Lamm, H.A. Gasteiger, Handbook of Fuel Cells — Fundamentals, Technology and Applications, John Wiley & Sons, Chichester, 2003.
[2] J. Scholta, J. Pawlik, N. Chmielewski, L. Jörissen, Journal of Power Sources 196 (2011) 5264—5271.
[3] C.A. Cottrell, S.E. Grasman, M. Thomas, K.B. Martin, J.W. Sheffield, International Journal of Hydrogen Energy 36 (2011) 7969—7975.
[4] B.C.H. Steele, A. Heinzel, Nature 414 (2001) 345—352.
[5] X. Li, Principles of Fuel Cells, Taylor & Francis, New York, 2006.
[6] N. Akhtar, A. Qureshi, J. Scholta, Ch. Hartnig, M. Messerschmidt, W. Lehnert, International Journal of Hydrogen Energy 34 (2009) 3104—3111.
[7] T.C. Wu, N. Djilali, Journal of Power Sources 208 (2012) 248—256.
[8] J. Kunes, Dimensionless Physical Quantities in Science and Engineering, Elsevier, 2012.
[9] J. Chen, B. Zhou, Journal of Power Sources 177 (2008) 83—95.
[10] D. Spernjak, A.K. Prasad, S.G. Advani, Journal of Power Sources 195 (2010) 3553—3568.
[11] J. Scholta, F. Häußler, H. Müller, L. Jörissen, ECS Transactions 26 (1) (2010) 89—94.
[12] J.H. Nam, M. Kaviany, International Journal of Heat and Mass Transfer 46 (2003) 4595—4611.
[13] Y. Wang, S. Basu, C.-Y. Wang, Journal of Power Sources 179 (2009) 603—617.
[14] J.E. Dawes, N.S. Hanspal, O.A. Family, A. Turan, Chemical Engineering Science 64 (2009) 2781—2794.
[15] M.A. Hickner, N.P. Siegel, K.S. Chen, D.S. Hussey, D.L. Jacobson, M. Arif, Journal of the Electrochemical Society 155 (2008) B427—B434.
[16] T. Sasabe, P. Deevanhxay, S. Tsushima, S. Hirai, Journal of Power Sources 196 (2011) 8197—8206.
[17] P. Deevanhxay, T. Sasabe, S. Tsushima, S. Hirai, International Journal of Hydrogen Energy 36 (2011) 10901—10907.
[18] M.M. Mench, Q.L. Dong, C.Y. Wang, Journal of Power Sources 124 (2003) 90—98.
[19] R.J. Bellows, M.Y. Lin, M. Arif, A.K. Thompson, D. Jacobson, Journal of the Electrochemical Society 146 (1999) 1099—1103.
[20] R. Satija, D.L. Jacobson, M. Arif, S.A. Werner, Journal of Power Sources 129 (2004) 238—245.
[21] Ch. Hartnig, I. Manke, N. Kardjilov, A. Hilger, M. Grünerbel, J. Kaczerowski, J. Banhart, W. Lehnert, Journal of Power Sources 176 (2008) 452—459.
[22] Ch. Tötzke, I. Manke, T. Arlt, H. Markötter, N. Kardjilov, A. Hilger, Ph. Krüger, Ch. Hartnig, J. Scholta, J. Banhart, Journal of Power Sources 196 (2011) 4631—4637.
[23] I. Manke, H. Markotter, C. Totzke, N. Kardjilov, R. Grothausmann, M. Dawson, C. Hartnig, S. Haas, D. Thomas, A. Hoell, C. Genzel, J. Banhart, Advanced Engineering Materials 13 (2011) 712—729.
[24] Ch. Hartnig, I. Manke, Encyclopedia of Electrochemical Power Sources (2009). pp. 738—757.
[25] N. Kardjilov, A. Hilger, I. Manke, M. Strobl, M. Dawson, S. Williams, J. Banhart, Nuclear Instruments and Methods in Physics Research Section A: Accelerators, Spectrometers, Detectors and Associated Equipment 651 (2011) 47—52.
[26] N. Kardjilov, A. Hilger, I. Manke, M. Strobl, M. Dawson, J. Banhart, Nuclear Instruments and Methods in Physics Research Section A: Accelerators, Spectrometers, Detectors and Associated Equipment 605 (2009) 13—15.
[27] J.G. Carton, V. Lawlor, A.G. Olabi, C. Hochenauer, G. Zauner, Energy 39 (2012) 63—73.
[28] S. Enz, J. Scholta, ANSYS Conference & 29th CADFEM User's Meeting (19—21 October 2011). Stuttgart.
[29] S. Enz, M. Messerschmidt, J. Scholta, Poster, 13th UECT (2012). Ulm.
[30] S.V. Patankar, Numerical Heat Transfer and Fluid Flow, Hemisphere, Washington, DC, 1980.
[31] J.H. Ferziger, M. Peric, Computational Methods for Fluid Dynamics, Springer-Verlag, Berlin, Heidelberg, New York, 2002.
[32] X. Li, I. Sabir, J. Park, Journal of Power Sources 163 (2007) 933—942.
[33] G.J.M. Janssen, M.L.J. Overfelde, Journal of Power Sources 101 (2001) 117—125.
[34] R.M. Kuhn, PhD thesis, University Ulm, 2011.
[35] Ph. Krüger, H. Markötter, J. Haussmann, M. Klages, T. Arlt, J. Banhart, Ch. Hartnig, I. Manke, J. Scholta, Journal of Power Sources 196 (2011) 5250—5255.
[36] R. Kuhn, J. Scholta, Ph. Krüger, Ch. Hartnig, W. Lehnert, T. Arlt, I. Manke, Journal of Power Sources 196 (2011) 5231—5239.
[37] J. Zhang, D. Kramer, R. Shimoi, Y. Ono, E. Lehmann, A. Wokaun, K. Shinohara, G.G. Scherer, Electrochimica Acta 51 (2006) 2715—2727.
[38] Ch. Hartnig, L. Jörissen, J. Kerres, W. Lehnert, J. Scholta, in: M. Gasik (Ed.), Materials for Fuel Cells, Woodhead Publishing, Cambridge, 2008, ISBN 978-1-84569-330-5.
[39] X. Yan, M. Hou, H. Zhang, F. Jing, P. Ming, B. Yi, Journal of Power Sources 160 (2006) 252—257.
[40] S. Cho, Y. Wang, K.S. Chen, Journal of Power Sources 206 (2012) 119—128.
[41] R. Anderson, D. Wilkinson, X. Bia, L. Zhang, Journal of Power Sources 196 (2011) 8031—8040.
[42] A.D. Le, B. Zhou, Electrochimica Acta 54 (2009) 2137—2154.
[43] B. Han, J. Yu, H. Meng, Journal of Power Sources 202 (2012) 175—183.